



CHORUS

This is the accepted manuscript made available via CHORUS. The article has been published as:

Active aerodynamic drag reduction on morphable cylinders

M. Gutttag and P. M. Reis

Phys. Rev. Fluids **2**, 123903 — Published 26 December 2017

DOI: [10.1103/PhysRevFluids.2.123903](https://doi.org/10.1103/PhysRevFluids.2.123903)

Active aerodynamic drag reduction on morphable cylinders

M. Guttag

*Department of Mechanical Engineering,
Massachusetts Institute of Technology,
Cambridge, MA 02139, USA*

P.M. Reis*

*Department of Mechanical Engineering,
Department of Civil and Environmental Engineering,
Massachusetts Institute of Technology,
Cambridge, MA 02139, USA*

(Dated: November 30, 2017)

We study a mechanism for active aerodynamic drag reduction on morphable grooved cylinders, whose topography can be modified pneumatically. Our design is inspired by the morphology of the Saguaro cactus (*Carnegiea gigantea*), which possesses an array of axial grooves, thought to help reduce aerodynamic drag, thereby enhancing the structural robustness of the plant under wind loading. Our analogue experimental samples comprise a spoked rigid skeleton with axial cavities, covered by a stretched elastomeric film. Decreasing the inner pressure of the sample produces axial grooves, whose depth can be accurately varied, on demand. First, we characterize the relation between groove depth and pneumatic loading through a combination of precision mechanical experiments and finite element simulations. Secondly, wind tunnel tests are used to measure the aerodynamic drag coefficient (as a function of Reynolds number) of the grooved samples, with different levels of periodicity and groove depths. We focus specifically on the drag crisis and systematically measure the associated minimum drag coefficient and the critical Reynolds number at which it occurs. The results are in agreement with the classic literature of rough cylinders, albeit with an unprecedented level of precision and resolution in varying topography using a single sample. Finally, we leverage the morphable nature of our system to dynamically reduce drag for varying aerodynamic loading conditions. We demonstrate that actively controlling the groove depth yields a drag coefficient that decreases monotonically with Reynolds number and is significantly lower than the fixed sample counterparts. These findings open the possibility for the drag reduction of grooved cylinders to be operated over a wide range of flow conditions.

* To whom correspondence should be addressed: preis@mit.edu.

I. INTRODUCTION

The *Carnegiea gigantea*, commonly known as the Saguaro cactus (Fig. 1a), is an iconic and endemic plant to the Sonoran desert in the American southwest. These cacti can grow to be 15 m tall with diameters over 0.8 m and weigh over 1800 kg [1, 2]. Despite their shallow root base, these essentially cylindrical plants are able to withstand wind speeds of up to 38 ms^{-1} without failure due to this aerodynamic loading and live as long as 150 years [3]. The surface morphology of a mature Saguaro cactus comprises between 10 and 30 vertical (axial) grooves that are equally spaced around its circumference [1]. The depth of these grooves varies along the trunk [4], and their shape also changes with the seasons [1]. During the wet season, the trunk undergoes hygroscopic swelling and the grooves are less pronounced. In reverse, during the dry season, the stored water is gradually consumed and the grooves deepen [1]. For a 1.5 m tall cactus, the ratio between groove depth and plant diameter has been measured to be approximately 0.07 [5]. A possible evolutionary advantage of the grooves is that they may provide additional structural support to the plant. Another prevailing hypothesis in the literature [4, 6] is that the axial corrugations are thought to yield an aerodynamic advantage that reduces the overall form drag on the structure. This drag reduction may then allow the plant to withstand high wind loads, for example, during storm conditions. In our current study, we do not set out to determine which hypothesis is correct. Instead we use the latter interpretation of the effect of the grooves on drag reduction as an original source of inspiration and motivation for our work.

Smooth cylinders under high Reynolds number flow conditions ($Re \gtrsim 2 \times 10^5$, taking the diameter as the characteristic length), are well-known to undergo a phenomena referred to as the *drag crisis* [7]. With increasing Re , the drag coefficient, C_d , first drops sharply (*critical regime*), until a minimum is reached at a critical Reynolds number, Re^* , after which C_d increases again (*supercritical regime*), before plateauing (*transcritical regime*) [8, 9]. This drop in drag is related to a delay in separation caused by a laminar-to-turbulent flow transition in the boundary layer. Roughening the surface of the cylinder causes the drag crisis to occur earlier by promoting the transition from a laminar to turbulent boundary layer [4, 9, 10]. Numerous past studies have investigated the influence of surface topography on the drag crisis of bluff bodies [9, 11–14]. For example, covering the surface of cylinders or spheres by sand grains to produce an uniformly random surface roughness has been shown to reduce their drag coefficient by as much as a factor of 1.8 (for cylinders) [9] or 5 (for spheres) [12], when compared to their smooth counterparts. Periodic patterns of dimples have also proven to be effective at reducing the drag on both spherical [11, 14] and cylindrical [13] bluff bodies.

Returning to the resilience of Saguaro cacti under wind loading, it has been proposed that the axial grooves on their surface have an effect similar to the aforementioned rough cylinders, thereby enhancing the aerodynamic performance of the plant [10]. This hypothesis inspired our work.

Also motivated by the cactus analogy, a series of previous studies have addressed the aerodynamics of cylinders with longitudinal grooves [4, 6, 10, 16–21]. For example, Refs. [4, 10] report experiments that explore the effect the surface shape (smooth, rough and cactus-shaped grooves) of cylinders at high Reynolds numbers ($2 \leq Re [\times 10^4] \leq 20$). In this study, the samples with v-shaped grooves (similar to those of cacti) were machined with a depth to cylinder

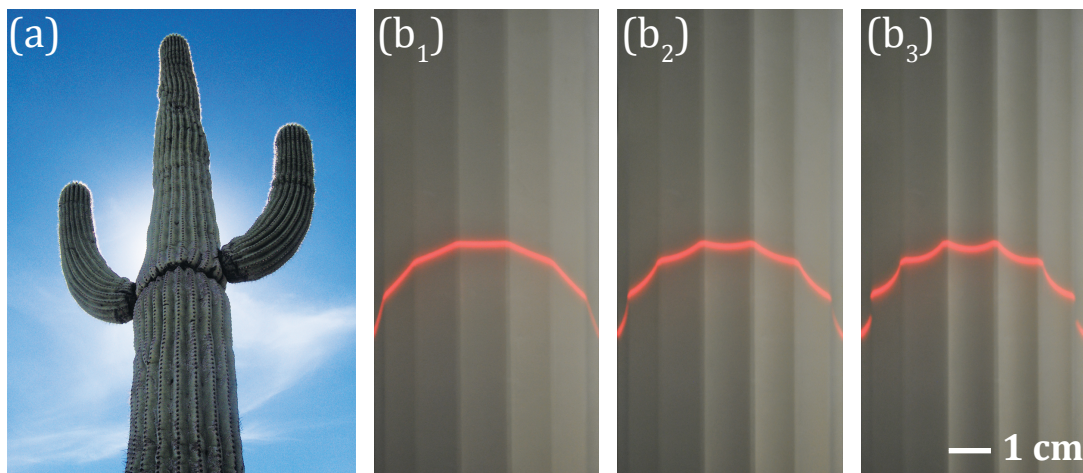


FIG. 1. (a) Representative photograph of a Saguaro cactus (Scottsdale, Arizona) [15]. (b) Photographs of a grooved cylindrical sample covered by a stretched latex film. The surface topography can be morphed pneumatically by increasing the pressure differential between the inside and the outside of the samples: (b1) $\Delta p = 1000 \text{ Pa}$, (b2) $\Delta p = 5000 \text{ Pa}$, (b3) $\Delta p = 10,000 \text{ Pa}$. A laser sheet aligned at 45° with respect to the cross section of the sample is used to measure the depth of the surface grooves.

diameter ratio spanning $0.035 \leq L/D \leq 0.105$. Within the tested range of Re , the grooved cylinders showed a monotonic increase in C_d with increasing Re , then asymptoting at values in the range $1.04 \leq C_d \leq 1.13$, depending on the groove depth (the deepest grooves providing the lowest C_d). This monotonic dependence indicates that all cases considered in these experiments were already in the supercritical and transcritical flow regimes (*i.e.*, the critical Reynolds number was below the explored range of Re ; $Re^* < 2 \times 10^4$) [4].

A subsequent experimental study [19] also examined the effect of the shape of grooves on C_d over range of Reynolds numbers ($1 \leq Re [\times 10^4] \leq 10$). These experiments used 48 mm diameter cylinders with 0.5 mm deep grooves of triangular and arc-shaped geometries. The results showed that both triangular and arc-shaped grooves induced the drag crisis at the same value of Re , but the triangular-grooved cylinders exhibited a lower value of the minimum drag coefficient [19]. A more recent study [21] focused on catenary shaped grooves in the critical Reynolds number regime ($2 \leq Re [\times 10^4] \leq 12$). The experiments were performed with cylinders of varying groove depth, width and area. Increasing the ratio, A^* , between the area of all the grooves and the area of the cylinder decreased the critical Reynolds number and increased the minimum drag coefficient. This finding was robust regardless of whether A^* was increased by increasing the groove depth, groove width or shape factor [21].

In addition to the shape of grooves, the effect of the number of grooves on the drag on cylinders (with triangular-shaped features) has also been investigated [20]. Samples with an increasing number of grooves (from 20 to 30) exhibited the drag crises at lower values of Re , and the drag crisis was characterized by a more gradual the drop, even if the minimum drag coefficient appeared unchanged [20].

Overall, combining the findings from the past studies mentioned above establishes that different groove patterns can change the aerodynamic performance of a cylinder. However, these investigations were limited in the range and extent of the explored parameter space by the time and cost needed to fabricate individual samples for each configuration. Additionally, each individually manufactured samples (with a fixed surface shape) minimizes the drag coefficient at a single value of Reynolds number, Re^* , whereas, for all other Re , the drag can be specifically higher. As such, an important shortcoming precluding the translation of this drag reduction mechanism with fixed topographies into engineering applications is that any aerodynamic enhancement is limited to relatively narrow ranges of Re .

Here, we study the aerodynamic performance of cylinders using a single, albeit morphable, sample whose topography that can be varied systematically and precisely, on demand. The tuning of the surface shape is accomplished by the pneumatic actuation of the flexible elastomeric film covering an inner rigid skeleton, with a single pressure signal that can be continuously varied. In Fig. 1b, we present representative photographs of a sample at three different states of pneumatic loading ($\Delta p = 1, 5$ and 10 kPa). Therefore, by varying the internal pressure of the sample, we can set the sample to numerous fixed groove shapes, specifically the groove depth. Wind tunnel tests are used to characterize the aerodynamic drag of our samples, over a wide range of Reynolds numbers, for each fixed depth. We determine which groove depth exhibits the lowest drag coefficient at any given Reynolds number. Finally we present a system in which the drag on the samples can be automatically minimized by changing the groove depth ‘*on the fly*’, depending on the measured velocity of the oncoming flow.

Our paper is organized as follows. In Section II, we describe our experimental apparatus used to measure the drag forces on the cylindrical samples, and detail the sample fabrication method. In Section III, we describe the finite element simulations and mechanical experiments used to study the mechanics of deformation of the outer elastomeric film and establish a relationship between the groove depth and the internal pressure in the samples. Next, the protocol of the wind tunnel experiments is presented in Section IV A. Finally, the results of the aerodynamic experiments are presented in Sections IV B and IV C.

II. THE EXPERIMENTS

Our cylindrical samples comprised a rigid acrylic skeleton covered by a stretched cylindrical film made of latex. The rigid skeleton contained a series of inner cavities set by an array of equally spaced radial spokes, aligned axially. Decreasing the internal pressure in the cavities caused the outer latex film to stretch further and, consequently, increase the depth of the axial grooves. Therefore, the topography of the samples could be tuned gradually and on-demand, through pneumatic actuation. These samples were then loaded aerodynamically in a flow field generated by a wind tunnel. The resulting drag force was measured directly by a precision system containing a load-cell. The velocity of the incoming flow was then varied systematically to determine the drag coefficient, C_d , over a range of Reynolds number ($2.5 < Re [\times 10^4] < 15$), and for different set values of the groove depth.

Next, we describe in more detail, first, the experimental apparatus and, then, the sample fabrication procedure.

A. Experimental apparatus

Fig. 2a shows a photographs of the experimental apparatus used throughout this investigation. The incoming air flow was produced by an open return wind tunnel with a $30.5 \times 30.5 \text{ cm}^2$ test section, which was capable of producing uniform steady flow speeds of $5 < U [\text{ms}^{-1}] < 34$, measured by a Pitot tube and a high accuracy capacitance manometer (690A Baratron, MKS Instruments). For all the values of U used in this study, the turbulence intensity, defined as fluctuations of the wind speed, were below 1% of the mean velocity. The flow direction was aligned with the y -axis (see the definition of the axes in Fig 2a). The cylindrical samples were mounted such that they spanned the width of the wind tunnel, along the x -direction, perpendicular to the incoming flow, and positioned at the vertical center of the test section. The sample protruded through holes in the y - z side walls of the test section.

The cylindrical samples were 43 cm long with a 3.5 cm radius (measured from the center of the cylinder to the extremity of one of the spokes). Circular caps made out of acrylic were inserted at both ends of the sample to ensure sealing. One of these endcaps (left-and side of Fig 2a) contained a port to connect the sample, via PVC tubing, to a vacuum pump (DOA-P704-AA, Gast). A high-resolution electronic pressure control valve (QPV1, Proportion-Air, Inc.) was introduced between the sample and the vacuum pump to automatically regulate the pressure of the system using a data-acquisition device (DAQ, USB-6008, National Instruments). This pressure control valve was then controlled by a custom LabVIEW program (LabVIEW 2010, National Instruments). The two endcaps of the sample were mounted onto a U-shaped aluminum frame, which was itself bolted to one end of a linear air bearing (RAB2, Nelson Air Corp.). The other end of the air bearing was connected to a precision load-cell (LRM200 Miniature S-Beam Load Cell, Futek). With this setup, aerodynamic drag forces exerted onto the grooved cylindrical samples could be measured in the range $0.05 < F_d \text{ N} \leq 22.2$.

Both the force and the wind velocity signals were digitized simultaneously by the DAQ system. The experimental setup detailed above allowed for the control of the internal pressure of the cylindrical samples (and thus the shape of the grooves), while simultaneously enabling measurement and recording of both the drag forces on the sample and the velocity of the incoming flow.

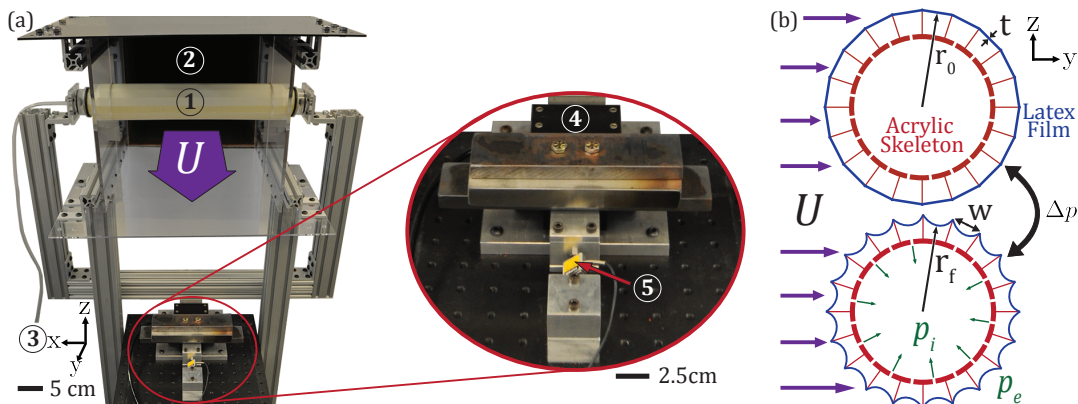


FIG. 2. (a) Photograph of the experimental apparatus used to measure the drag force on a grooved cylindrical sample under aerodynamic loading. The sample (1), mounted across the wind tunnel (2), is rigidly connected to a force sensor (5) via an air bearing (4) to measure the exerted aerodynamic drag forces. The internal pressure of the sample is set by a regulated vacuum pressure source (3). The air flow with average far-field speed U is aligned perpendicularly to the axis of the sample. (b) Schematic diagram of the cross-section of the sample (top) comprising a rigid acrylic skeleton (red) covered by a thin latex film (blue, thickness $t = 0.25 \text{ mm}$). Depressurizing (Δp) the inner cavity of the shell results in deeper grooves (bottom).

B. Fabrication of the samples

In Fig. 2b, we present a schematic diagram of the cross-section of our cylindrical samples, which were custom fabricated. The samples consisted of a latex film (represented by the blue line in Fig. 2b) stretched over a rigid acrylic skeleton (represented by the red circle with spokes in Fig. 2b).

To manufacture the rigid skeleton, first, spokes with a height of 9.5 mm were laser cut (Laser Pro, Spirit GLS) out of 1.6 mm thick acrylic plates. Second, a series of rectangular holes were laser-cut on the surface of an acrylic tube (50.8 mm outer diameter and 3.175 mm wall thickness). There were two sets of holes cut into the base tube. The first

set was uniformly spaced around the circumference of the cylinder and were subsequently plugged with the spokes to create the skeletal structure, with an outer diameter of 69.8 mm. The second set of holes was cut to allow air to flow between the inside of the tube and the cavities created beneath the latex film (more below). This allowed for the pressure to equalize inside the base tube and in the cavities. The spacing between the ends of two neighboring spokes, w , depended on the number of grooves in the sample. In our experiments we used samples with $N = \{14, 16, 20, 24\}$ grooves (*i.e.*, $w = \{15.5, 13.6, 10.9, 9.1\}$ mm, respectively).

Thin latex sheets (McMaster-Carr, part # 8611K13, thickness $t = 0.25$ mm and shear modulus $G = 577 \pm 32$ kPa) were cut into rectangles, and the ends glued together to form tubular shells with 50.8 mm diameter. The latex film was then stretched over the acrylic skeleton and the ends were sealed with o-rings. The resulting value of the prestretch (defined as the ratio between the perimeter of the latex film after and before stretching over the skeleton) depended on the number of grooves of the sample: $\lambda = \{1.364, 1.366, 1.369, 1.371\}$ for $N = \{14, 16, 20, 24\}$, respectively. These values of pre-stretch were chosen to ensure that no fluttering of the latex membrane was observed in the wind-tunnel experiments (Section IV B), especially in the upper range of Reynolds numbers explored, where vortex-induced vibrations were otherwise possible.

The elastic properties of the latex films (needed for the Finite Element Simulations detailed in Section III, below) were determined using an universal testing machine (5943, Instron). Dog bone specimens (ASTM D412 type A and B) were laser-cut from the same latex material used to make the samples, and tested under uniaxial tension. The experimental data for the engineering stress versus stretch obtained from the tensile test were then fitted to a Gent constitutive model [22]. This model is widely used to describe elastomeric materials under large deformation and involves three parameters: two elastic coefficients, C_1 and C_2 , and one coefficient, J_m , related to the maximum stretch ratio. The two elastic coefficients can be used to estimate the shear modulus, G , of the material. From the fitting of the Gent model to the stress-stretch data we obtained: $J_m = 37.5 \pm 1.7$, $C_1 = 115.7 \pm 5.7$ kPa, $C_2 = 518.0 \pm 30.2$ kPa and $G = 577 \pm 32$ kPa.

III. MECHANICS OF DEFORMATION OF THE GROOVED SURFACE

In this section, we present the results of both mechanical experiments and finite element (FE) simulations used to characterize how the shape of the grooves, specifically the groove depth, d , depends on the internal pressure, Δp . This relationship between d and Δp will be required later (Section IV) to inform the wind tunnel experiments. In Fig. 2b, we show a schematic diagram of a segment of the latex film suspended above a single cavity of the rigid skeleton. When the value of the pressure inside the cavity, p_i , is smaller than the exterior pressure, p_e , the pressure differential, $\Delta p = p_e - p_i$, loads the latex film. This loading causes the film to deform inward and, thus, deepen the surface groove. To study the mechanics of deformation of the film, we performed a series of experiments where Δp was fixed to a set value and a laser sheet was then projected onto its surface, at a 45° angle relative to the central axis of the cylinder. Photos were taken of the resulting line of illumination, representative examples of which are shown in Fig. 1b. From these photographs, we extracted the height profile of the grooves, using a custom image processing code (Matlab).

Along with the physical experiments, we performed Finite Element Modeling (FEM) using Abaqus/Standard 6.14.

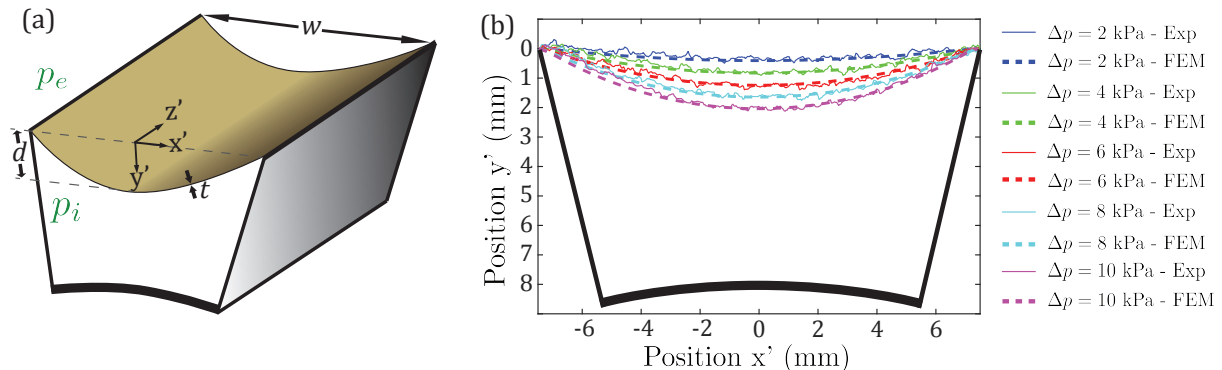


FIG. 3. (a) Schematic diagram of a single groove after applying the pneumatic loading by setting the pressure differential to Δp . The groove depth, width and film thickness are represented by d , w and t , respectively. (b) Results of experiments (solid lines) and FEM simulations (dashed lines) showing the shape of the surface of the latex film at increasing values of $\Delta p = \{2, 4, 6, 8, 10\}$ kPa, for a sample with $N = 14$ grooves. The rigid (acrylic) skeleton is represented by the thick black lines. Given the periodicity of the system, only the data for a single groove is shown.

Given the axial symmetry of the system, the model was simplified to a single two-dimensional (2D) groove section (shown in Fig. 3). The acrylic skeletal structure was simulated with rigid elements, while the film was simulated with 2D solid elements (CPE4H). A convergence study was performed, which led to the selection of a regular mesh with 150 elements along the arc-length of the latex film, and 8 elements along its thickness. The simulation protocol was as follows: (i) first, the film was preconditioned by deforming it to appropriate value of prestretch ($\lambda = \{1.364, 1.366, 1.369, 1.371\}$ for the samples with $N = \{14, 16, 20, 24\}$, respectively); (ii) then, a uniform negative pressure was applied to the inner surface of the film, so that the pressure differential was increased linearly from $\Delta p = 0$ to $\Delta p = 10$ kPa. This pneumatic loading was implemented as a live pressure, such that the force was always applied normal to the surface.

In Fig. 3b, we show examples of the experimental and computed surface profiles of a single groove, at five different values of the internal pressure ($\Delta p = \{2, 4, 6, 8, 10\}$ kPa), for a sample with $N = 14$ grooves. The groove profiles closely resemble catenaries, especially for small values of Δp , which is to be expected given the nearly radial pneumatic loading on the latex film. We find excellent agreement between the experiments and the FEM simulations, noting that the latter involve no free fitting parameters.

From the groove profiles, a representative set of which was shown in Fig. 3, we measure the groove depth as $d = r_o - r_f$, where r_o and r_f are defined in Fig. 2b, and d is drawn schematically in Fig. 3a. It is worth noting that the groove depth, d , is defined relative to the initial state of the sample with no pressure being applied. This means that for a sample with N grooves, $d = 0$, corresponds to an N -sided polygon rather than a perfect cylinder. However, for increasing values of N , the sample approaches the a smooth cylinder case. In Fig. 4a, we plot d versus Δp , for four different samples with $N = \{14, 16, 20, 24\}$, from both the experiments and the corresponding FEM simulations; excellent agreement is found between the two. The errorbars on the experimental data represent the standard deviation of five different tests. We find a linear relationship between the groove depth and the internal pressure. The constant of proportionality decreases for the samples with increasing N . This is likely due to the difference in stretch required to reach the same groove depth in samples with more grooves. Given a constant groove depth, samples with higher N achieve a higher stretch than those with fewer grooves. Thus, a larger load, *i.e.* Δp , must be applied to samples with more grooves.

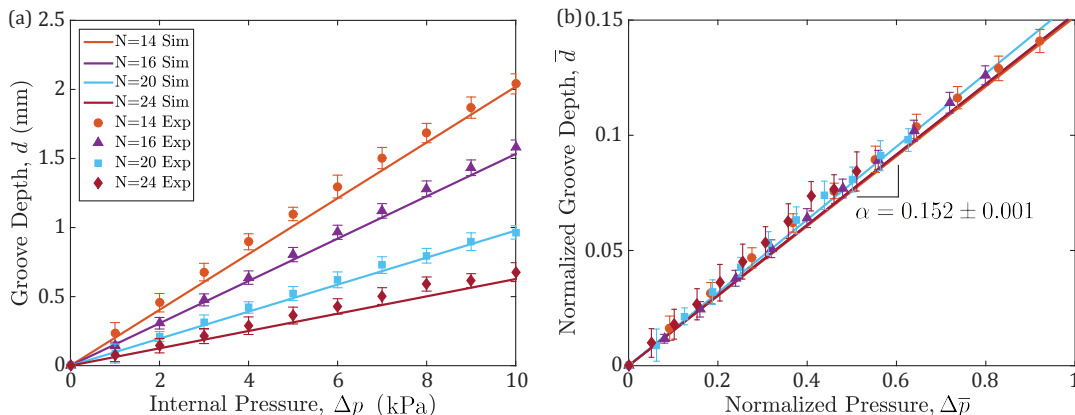


FIG. 4. (a) Groove depth, d , versus pressure differential, Δp , for samples with different numbers of grooves; see legend, which also applies to (b). Solids lines and data points correspond to simulations and experiments, respectively. (b) Normalized groove depth, $\bar{d} = d/w$, as a function of normalized pressure, $\Delta \bar{p} = \Delta p w / [Gt]$, for the same data as in (a). The slope of the best linear fit to the data is $\alpha = 0.152 \pm 0.001$.

Next, we nondimensionalize the groove depth as $\bar{d} = d/w$, and the pressure as $\Delta \bar{p} = \Delta p w / [Gt]$. The latter was chosen based on dimensional analysis. In Fig. 4b, we plot these dimensionless quantities and find that all the experimental and numerical data collapse onto a linear master curve, for all of the samples tested:

$$\bar{d} = \alpha \Delta \bar{p}, \quad (1)$$

where $\alpha = 0.152 \pm 0.001$ was determined by fitting the data.

Thus far, our results establish a predictive relationship between the groove depth and the internal pressure of the samples. This, together with the electronic pressure control valve, we are able to set and vary the depth of the grooves on demand. This capability was used in the subsequent wind tunnel experiments to systematically characterize the dependence of the aerodynamic performance of our samples, specifically the drag coefficient, on the groove depth. The details and results of these experiments are addressed next.

IV. WIND TUNNEL TESTS

Above, through mechanical experiments and FEM simulations, we established a relationship between the depth of the grooves and the internal pressure of the samples. We proceed by characterizing the aerodynamic performance of our grooved samples using wind tunnel tests. More specifically, we shall systematically quantify how the aerodynamic drag coefficient of the samples, C_d , varies with the Reynolds number of the flow (in the range $2.5 < Re [\times 10^4] < 15$), as a function of the groove depth, d .

Two types of experiments were undertaken with either (i) *fixed* or (ii) *active* grooves. (i) For the *fixed groove experiments*, we measured C_d across the full range of Re , while setting the internal pressure of the sample at a fixed value, to target a constant value of d . In doing so, we followed the mechanical design principles identified in Section III that relate d with Δp . For each value of d , we tabulated the corresponding minimum value of C_d and the critical Re^* at which it occurred. (ii) Additionally, we performed *active groove experiments* where the Reynolds number was gradually increased, and at each Re , the groove depth was automatically adapted to minimize the drag coefficient. As we shall show below, these morphable cylinders with an active control of their groove depth exhibited an overall aerodynamic drag, across the full range of Re , that was significantly lower than any of their fixed counterparts.

A. Experimental protocol to measure the aerodynamic drag coefficient

During testing, the groove depth of the samples was set by varying the internal pressure through the vacuum regulator as described in Section II A. The groove depth was varied from $d = 0$ to $d = 0.81$ mm (*i.e.*, $\bar{d} = d/w = 0.1$ in dimensionless form), for four samples with the following numbers of grooves: $N = 14, 16, 20$ and 24 . The wind speed was then slowly increased at a rate of $\dot{U} \approx 0.05$ m/s², until either the wind speed reached a maximum (at $U = 34$ ms⁻¹) or the signal from load-cell became saturated (at $F_d = 22.25$ N).

Based on the measured quantities, we calculated the Reynolds number as:

$$Re = \frac{UD}{\nu}, \quad (2)$$

where $D = 6.98$ cm is the outer diameter of the sample, and $\nu = 1.57 \times 10^{-5}$ m²s⁻¹ is the kinematic viscosity of air (at 25°C). Moreover, the drag coefficient was calculated as:

$$\bar{C}_d = \frac{2F_d}{\rho U^2 LD}, \quad (3)$$

where $\rho = 1.18$ kg m⁻³ is the density of air (at 25°C), and $L = 30.5$ cm is the width of the wind tunnel. All experiments were performed in the range $2.5 < Re [10^4] < 15$, over which, the measured drag force laid within $0.3 < F_d [\text{N}] < 17$.

It is important to note that the projected area of the sample is relatively large compared to the cross-sectional area of the test section of wind tunnel; the blockage ratio is $\beta = DL/L^2 = 0.23$. As such, blockage effects [23] need to be taken into account. Otherwise, calculating the drag coefficient directly from Eq. (3) would lead to artificially high values. In order to compensate for this blockage, Maskell's theory [24] was used to *correct* the measured drag coefficient as:

$$C_d = \frac{\bar{C}_d}{1 + \epsilon \beta \bar{C}_d}, \quad (4)$$

where \bar{C}_d is the *uncorrected* drag coefficient [from Eq. (3)] and $\epsilon = 0.3453$ is a numerical factor determined using the following fitting protocol. Wind tunnel experiments were first performed using four smooth, rigid cylinders of diameters $D = \{1.90, 3.81, 6.35, 7.62\}$ cm, in the range of Reynolds number, $2.5 < Re [10^4] < 15$. The results of these experiments are shown in Fig 5.

Throughout this range of Re , our smooth cylinders, unlike the grooved samples, remained in the subcritical regime (*i.e.* prior to the drag crisis), where the drag coefficient for a smooth cylinder is well-known to be 1.2 [7]. As expected, for all the diameters tested experimentally, the \bar{C}_d calculated through Eq. (3) were consistently above this classic value. We then took the experimental data for $\bar{C}_d(Re)$, displayed as the solid symbols in Fig. 5, and calculated C_d through Eq. (4), while taking ϵ as a free fitting parameter. In the fitting procedure, we minimized the difference $|\langle \bar{C}_d \rangle - 1.2|$, using the `fminsearch` algorithm in Matlab [25], where $\langle \cdot \rangle$ represents averaging over the full Re range. In the fitting procedure, the uncorrected drag coefficients of all of the cylinders were considered simultaneously in order to attain a single value of ϵ that applied to all the samples by minimizing the total difference from the expected classic value of 1.2. This procedure yielded $\epsilon = 0.3453$. The open symbols in Fig. 5 represent the drag coefficients for each sample

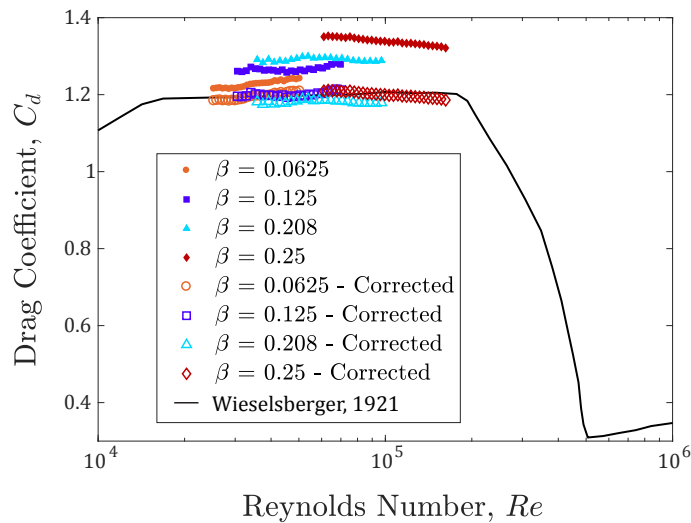


FIG. 5. Drag Coefficient, C_d , versus Reynolds number, Re , for smooth cylinders of different diameters and thus blockage ratios ranging from $1.90 < D [\text{cm}] < 7.62$ and $0.0625 < \beta < 0.25$, respectively. The solid black corresponds to the classic curve for a smooth cylinder [7]. The solid symbols are the uncorrected experimental results, and the open symbols are the corrected results using Maskell's theory [24] with $\epsilon = 0.3453$, which was determined using the procedure described in the text.

when this particular value of ϵ is used for the blockage correction. As a result all four cylinders used in this calibration, upon correction, exhibited the same value of $C_d \approx 1.2$. For the remainder of this study, we will report aerodynamic drag coefficients corrected through Eq. (4), with this specific value of ϵ , to take blockage effects into account.

B. Aerodynamic drag coefficient versus Reynolds number for the fixed grooved samples

In Fig. 6a, we plot a family of curves of the measured (and corrected for blockage effects) drag coefficient, C_d , as a function of Reynolds number, Re , for a sample with $N = 24$ grooves. The curves represent the sample in several fixed states with normalized groove depth in the range $0 \leq \bar{d} \leq 0.093$, at equally spaced increments of $\bar{d} = 0.0072$. The classical results for smooth cylinders by Wieselsberger [7] are also plotted (solid black line). For this smooth cylinder case, in the range of $2 \leq Re [10^4] \leq 20$, the drag coefficient is constant, at 1.2. The onset of the drag crisis occurs at $Re \approx 2 \times 10^5$, after which C_d drops dramatically for increasing Re until it reaches the minimum of $C_d = 0.3$ at $Re = 5 \times 10^5$. Hereon, we refer to the lowest value of the drag coefficient and the critical Reynolds number at which it occurs as C_d^* and Re^* , respectively.

For the shallowest groove depth ($\bar{d} = 0$), the drag coefficient in the subcritical regime decreases slowly from $C_d = 1.24$ to 1.17 over the range $2.5 \leq Re [10^4] \leq 7$. This indicates that in the subcritical regime, the drag on the samples starts slightly higher than that on a smooth cylinder, presumably due to the slightly non-circular cross section. The fixed sample also deviates from the smooth cylinder in terms of the value of Reynolds number for the onset of the drag crisis: $Re = 7 \times 10^4$ for the fixed grooves sample with $\bar{d} = 0$, and $Re = 20 \times 10^4$ for the smooth cylinder. For this fixed case, past the initiation of the drag crisis, C_d decreases for increasing Re , but never reaches a minimum. This means that for the fixed groove depth of $\bar{d} = 0$, the critical Reynolds number is above the maximum Reynolds number that we could explore experimentally, $Re^* > 1.5 \times 10^5$.

As the groove depth is systematically increased, the dependence of drag coefficient versus Reynolds number changes dramatically. Focusing on $\bar{d} = 0.043$, the drag crisis begins at approximately $Re = 2.75 \times 10^4$ and the drag coefficient drops sharply until reaching a minimum drag coefficient of $C_d^* = 0.75$, at $Re^* = 4.85 \times 10^4$. As the Reynolds number is increased further, the drag coefficient increases until asymptoting at $C_d = 0.9$. For experimental runs with deeper grooves, *e.g.* $\bar{d} = 0.093$, the $C_d(Re)$ curve is starkly different from the cases with shallower grooves. The drag coefficient first increases monotonically with Re , but eventually asymptotes to $C_d = 1.1$. This behavior points to the fact that for this particular value of the groove depth ($\bar{d} = 0.093$), the critical Reynolds number is lower than the lower bound of the available experimental range, *i.e.* $Re^* < 2.5 \times 10^4$. While the curves for the extreme values of \bar{d} appear to take on a very different shape than those for smaller \bar{d} , it is likely that, if the experimental range of Re could be expanded to both lower and higher bounds, then all the samples would show a clear subcritical, critical, supercritical and transcritical regime.

The above results (for $N = 24$ grooves) indicate that as \bar{d} increases, Re^* decreases, whereas C_d^* increases. This

trend also holds for samples with different number of grooves. In Fig 7a, we plot C_d^* versus \bar{d} , for samples with $N = 14, 16, 20$ and 24 grooves. For all of these cases, C_d^* increases with increasing \bar{d} . Moreover, for a given value of \bar{d} , samples with increasing N exhibit a decreasing value of C_d^* . Note that, even though $C_d^* \lesssim 0.9$ for all the data shown in Fig 7a, this is not necessarily the absolute maximum value of the C_d^* for these samples since only curves with a well-defined minimum were considered in our analysis. As described above for the case with $(N, \bar{d}) = (24, 0.093)$, samples with grooves deeper than those plotted in Fig 7 exhibit a monotonically increasing C_d with Re , without a clear minimum (the drag crisis occurs below the experimentally available range).

Fig. 7b shows the critical Reynolds number as a function of groove depth, for samples with different values of N . We find that Re^* decreases with \bar{d} for all cases. It is interesting to note that while there does not seem to be a trend with N , the data for each sample is consistent with a power-law scaling, $Re^* \sim \bar{d}^{-0.5}$, as is made more clear in the double-logarithmic plot in the inset of Fig. 7b.

The results presented thus far for the $C_d^*(\bar{d})$ and $Re^*(\bar{d})$ behavior are in agreement with the classic work of Achenbach [9] on the effect of surface roughness on drag coefficient for smooth cylinders. In his seminal studies, cylinders with different levels of roughness were fabricated by gluing sand grains of different sizes to the surface of cylinders. His studies defined a roughness coefficient as k_s/D , where k_s is the sand-grain roughness and D is the cylinder diameter. The results showed that increasing the roughness coefficient decreased the critical Reynolds number, and increased the minimum drag coefficient [9]. In our experiments the groove depth is analogous to the sand-grain roughness. For sake of comparison with Achenbach's data, Figs. 7c and 7d show $C_d^*(d/D)$ and $Re^*(d/D)$, respectively. Both Achenbach's work [9] and our own, demonstrate that at each Reynolds number there is a specific groove depth (or roughness in Achenbach's case) which minimizes drag. However, unlike Achenbach's work, which required a separate sample for each value of roughness, we can obtain a family of curves for different groove samples with a single sample. This makes it possible to more readily and systematically gather data for a large number of surface shapes. Being able to explore a larger number of groove depths allowed for the determination of the drag minimizing groove depth at each value of Re . This relationship will be leveraged next to actively control the sample, such that, given variable wind loading conditions, the groove depth can be automatically varied to minimize the aerodynamic drag.

C. Minimal aerodynamic drag from active pneumatic control of the surface deformation

The active system used to minimize the drag under changing conditions involved combining all of the results presented thus far. First, in Section IV B, we determined the groove depth which minimized the drag coefficient, at each Reynolds number. To set the groove depth to the optimal value, the corresponding internal pressure was determined according to the relationships found in Section III. Combining these we find the internal pressure required to minimize C_d at each Reynolds number. Therefore, an experimental control system was developed to actively change the surface morphology to minimize the drag coefficient. This system used the wind velocity data measured by the

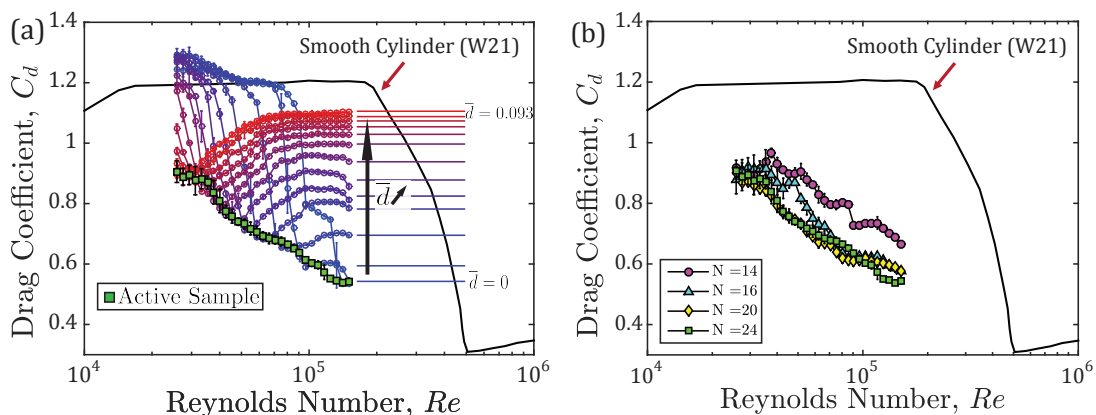


FIG. 6. Drag Coefficients, C_d , versus Reynolds number, Re , for grooved cylinders at increasing values of depressurization (and consequently increasing normalized groove depth, \bar{d}). Solid black line correspond to the result for a smooth cylinder (W21: [7]). (a) Fixed samples with $N = 24$ grooves at increasing values of normalized groove depth, \bar{d} (circles) and actively controlled sample (squares). The fixed samples range in groove depth from $\bar{d} = 0$ to 0.093 in equally spaced increments of $\bar{d} = 0.0072$. (b) Actively controlled samples with $N = 14$ (circles), $N = 16$ (triangles), $N = 20$ (diamonds) and $N = 24$ (squares).

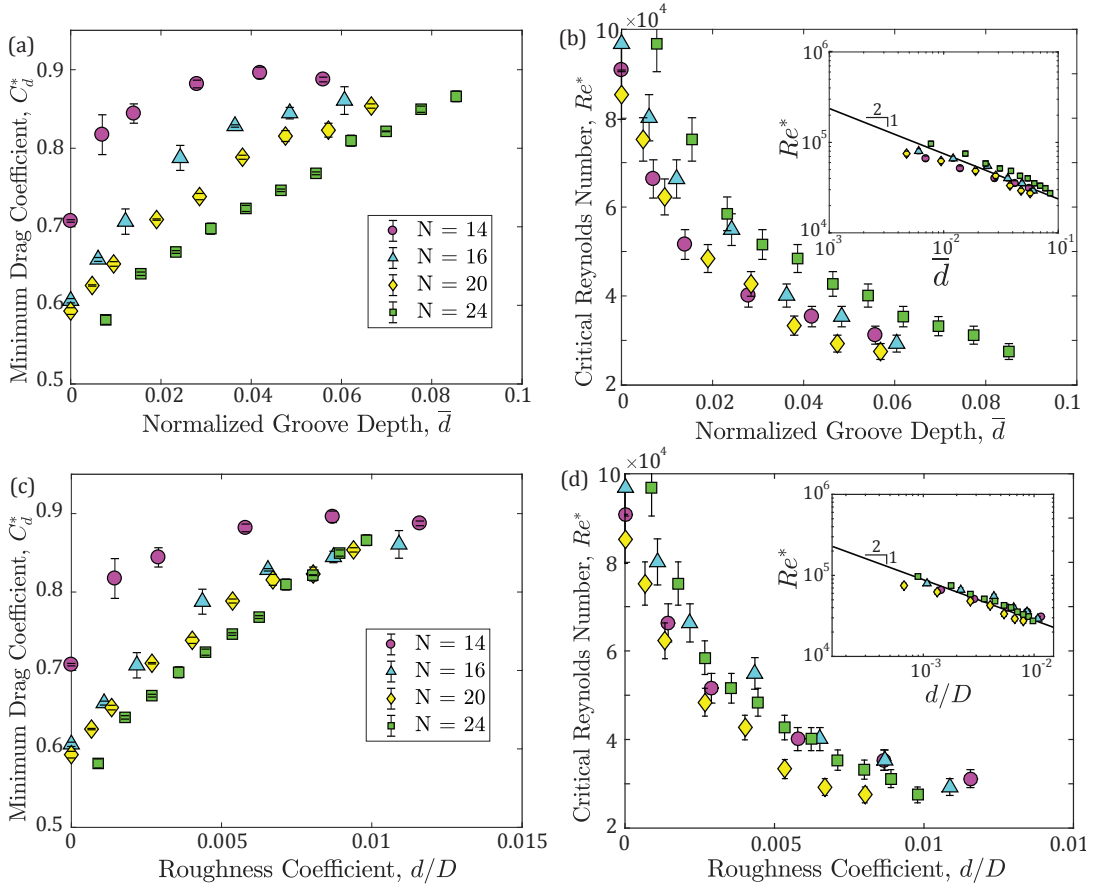


FIG. 7. (a) Minimum drag coefficient, C_d^* , of each $C_d(Re)$ curve in Fig. 6a, versus normalized groove depth, \bar{d} for samples with different numbers of grooves (see legend). (b) Critical Reynolds number, Re^* , versus normalized groove depth, \bar{d} , for the same samples used in (a). Inset: Log-log version of the same data suggesting consistency with the power-law scaling $Re^* \sim \bar{d}^{-1/2}$ (solid line)

pitot tube (and therefore Re) and then employed the relationship described above to set Δp in the sample to target the drag minimizing value.

The green squares in Fig. 6a show experimental data obtained using this active drag minimizing mechanism, demonstrating that the drag coefficient can be reduced significantly and consistently when compared to the fixed surfaces. This minimal behavior is achieved by essentially *surfing the wave* of minimum drag coefficient $C_d^*(Re)$. As such, the behavior of the active sample is a lower bound envelope of all of the fixed samples for different values of \bar{d} . Across the full range of Reynolds number explored ($2.5 \leq Re [10^4] \leq 15$), the drag coefficient of the active samples decreases monotonically from $C_d = 0.90$ to 0.54, which is in stark contrast to the highly non-monotonic behavior of the fixed samples (due to the presence of the drag crises).

Fig. 6b reproduces the data in Fig. 6a (for the active sample with $N = 24$), but now also adding the results for the active samples with $N = 14, 16$, and 20. For clarity, the $C_d(Re)$ curves of the corresponding static samples have not been included. Both active samples with $N = 20$ and $N = 24$ exhibit similar behavior in which there is a steady monotonic decrease in C_d with increasing Re . For the active sample with $N = 16$ the relationship $C_d(Re)$ is less smooth than the other samples. Moreover, for lower Reynolds numbers (around $2.5 < Re [10^4] < 6$), the drag coefficient for this $N = 16$ case is higher than the samples with a higher number of grooves. Reducing the number of grooves further to $N = 14$, the relationship $C_d(Re)$ becomes even less smooth and the drag coefficient is higher across the full range of Re . Given this, larger values of N seem to enhance the performance of the samples up to a point, beyond which increasing N has no effect.

It is important to remember that the initial state of each sample is an N -sided polygon due to the fact that the latex film is stretched over the rigid acrylic skeleton. When N is sufficiently large, the geometry is closer to a rough cylinder, with a roughness that can be pneumatically tuned. However, when N is small, such as in the case of $N = 14$, the geometry becomes far too discrete for the system to behave as a rough cylinder. We believe that this is the reason

why the $N = 14$ active sample has a $C_d(Re)$ behavior that is significantly less smooth than the other samples with more grooves.

V. CONCLUSION

In summary, we have experimentally investigated the aerodynamic performance of morphable grooved cylinders, whose surface topography can be varied through pneumatic actuation. We focused on how the dependence of the aerodynamic drag of samples with different groove depth and numbers, as a function of the velocity of the incoming flow (in high Reynolds number conditions). The surface topography of each sample, namely the depth of the grooves, could be systematically and dynamically varied by applying a pressure differential across the outer latex shell.

A series of mechanical experiments, combined with finite element simulations, demonstrated that the groove depth varied linearly on the pressure differential. Moreover, nondimensionalizing the groove depth yield a collapse of the data into a linear master curve, independently of the number of grooves. This master curve was later used as a design guideline and, part of a control system, to set the groove depth, on demand.

Our morphable cylindrical samples were then systematically tested in wind tunnel experiments. First, we tested samples with fixed grooves (*i.e.*, setting and then holding Δp constant for the full sweep of Reynolds number, during a single experimental run). These experiments showed that the drag coefficient, C_d , versus Reynolds number, Re , curves depended strongly on groove depth. These results are in agreement with classic experiments on rough cylinders [9], albeit with our added advantage of being able to systematically and precisely vary groove depth with a single sample. For samples with deeper grooves, the drag crisis occurs at lower values of the critical Reynolds number, Re^* , and with a higher value of the minimum drag coefficient, C_d^* .

From these experiments with fixed grooves, we determined the optimal groove depth for a given Reynolds number. With this information at hand, we then introduced an active control system that sensed the incoming wind speed and set the corresponding optimal groove depth to minimize the aerodynamic drag. We demonstrated that the actively morphable samples exhibited a drag that was consistently and significantly lower than the fixed sample counterparts, decreasing monotonically from $C_d = 0.90$ at $Re = 2.5 \times 10^4$ to $C_d = 0.54$ at $Re = 15 \times 10^4$. This monotonic behavior is in contrast with the strongly non-monotonic behavior of rough cylinders, or samples with fixed groove depth.

It should be noted that since we use a pneumatic system to control our samples, the pressure field on the surface of the samples resulting from the flow could potentially affect the geometry of the latex membrane in the specimens. However, throughout all of our experiments, the maximum stagnation pressure is at most 710 Pa, and this value is only reached at the extreme upper limit of the Reynolds numbers explored. Given that the pneumatic loading of the samples involves a pressure differential that is significantly higher (typically higher $\Delta p > 1$ kPa) than the stagnation pressure, we assumed that the pressure imposed by the flow field has effectively no effect in modifying the resultant geometry of the sample.

We believe that our active mechanism for aerodynamic drag reduction opens exciting opportunities for applications in bluff structures where aerodynamic performance under variable flow conditions is a primary concern for structural resilience or fuel efficiency. In this work, the closest that the samples could come to a smooth cylinder was a polygonal shape (even if closer to a circular cross-section for increasing values of N). Future work could explore samples that are able to reach a smooth cylinder, and thus recover the classical results while also having the functional benefits that we have presented. Additionally, building on our proof-of-concept investigation, future studies should address more complex geometries beyond the cylinders that we have studied. Moreover, specific applications may call for modes of actuation beyond pneumatics, such as particle-enhanced soft composites [26], shape memory polymers [27], or electroactive materials [28].

ACKNOWLEDGEMENTS

This research was conducted with Government support under and awarded by DoD, Air Force Office of Scientific Research, National Defense Science and Engineering Graduate (NDSEG) Fellowship, 32 CFR 168a and by the National Science Foundation (CAREER CMMI-1351449).

-
- [1] C. Hodge, *All about Saguaros* (Arizona Highways, Phoenix, 1991).
 - [2] L. Benson, *The Cacti of Arizona* (University of Arizona Press, Tucson, 1981).

- [3] H.C. Bulk, “The maximum daily wind gust speed climatology at Sky Harbor Airport, Phoenix, Arizona,” Laboratory of Climatology, Arizona State Univ. Report 18, 1984.
- [4] S. Talley and G. Mungal, “Flow around cactus-shaped cylinders,” Center for Turbulence Research Annual Research Briefs , 363 – 376 (2002).
- [5] G.N. Geller and P.S. Nobel, “Cactus ribs: influence on PAR interception and CO₂ uptake,” *Photosynthetica* **18**, 482–494 (1984).
- [6] P. Babu and K. Mahesh, “Aerodynamic loads on cactus-shaped cylinders at low reynolds numbers,” *Phys. Fluids* **20**, 035112 (2008).
- [7] C. Wieselsberger, “Neuere Feststellungen uber die Gesetze des Flussigkeitsund Luftwiderstandes,” *Physikalische Zeitschrift* **22**, 321–328 (1921).
- [8] A. Roshko, “Experiments on the flow past a circular cylinder at very high Reynolds number,” *J. Fluid Mech.* **10**, 345–356 (1961).
- [9] E. Achenbach, “Influence of surface roughness on the cross-flow around a circular cylinder,” *J. Fluid Mech.* **46**, 321–335 (1971).
- [10] S. Talley, G. Iaccarino, G. Mungal, and N. Mansour, “An experimental and computational investigation of flow past cacti,” Center for Turbulence Research Annual Research Briefs , 51 – 63 (2001).
- [11] D. Terwagne, M. Brojan, and P.M. Reis, “Smart Morphable Surfaces for Aerodynamic Drag Control,” *Adv. Mater.* **26**, 6659–6659 (2014).
- [12] E. Achenbach, “The effects of surface roughness and tunnel blockage on the flow past spheres,” *J. Fluid Mech* **65**, 113–125 (1974).
- [13] P.W. Bearman and J.K. Harvey, “Control of circular cylinder flow by the use of dimples,” *AIAA J.* **31**, 1753–1756 (1993).
- [14] P.W. Bearman and J.K. Harvey, “Golf Ball Aerodynamics,” *Aeronaut. Quart.* **27**, 112–122 (1976).
- [15] Wikimedia Commons/Public Domain: <https://commons.wikimedia.org/wiki/File:Saguaro3.jpg>.
- [16] J.E. Abboud, W.S. Karaki, and G.F. Oweis, “Particle Image Velocimetry Measurements in the Wake of a Cactus-Shaped Cylinder,” *J. Fluid Eng.* **133**, 094502 (2011).
- [17] A.M. El-Makdah and G.F. Oweis, “The flow past a cactus-inspired grooved cylinder,” *Exp. Fluids* **54**, 1464 (2013).
- [18] T. Kimura and M. Tsutahara, “Fluid dynamic effects of grooves on circular cylinder surface,” *AIAA J.* **29**, 2062–2068 (1991).
- [19] Y. Yamagishi and M. Oki, “Effect of Groove Shape on Flow Characteristics around a Circular Cylinder with Grooves,” *J. Vis.* **7**, 209–216 (2004).
- [20] Y. Yamagishi and M. Oki, “Effect of the number of grooves on flow characteristics around a circular cylinder with triangular grooves,” *J. Vis.* **8**, 57–64 (2005).
- [21] S.J. Quintavalla, A.J. Angilella, and A.J. Smits, “Drag reduction on grooved cylinders in the critical Reynolds number regime,” *Exp. Therm. Fluid Sci.* **48**, 15–18 (2013).
- [22] A.N. Gent, “Elastic instabilities in rubber,” *Int. J. Nonlinear Mech.* **40**, 165–175 (2005).
- [23] J. Anthoine, D. Olivari, and D. Portugaels, “Wind-tunnel blockage effect on drag coefficient of circular cylinders,” *Wind Struct.* **12**, 541–551 (2009).
- [24] E.C. Maskell, “A Theory of the Blockage Effects on Bluff Bodies and Stalled Wings in a Closed Wind Tunnel,” Aeronautical Research Council (Great Britain), R&M Report No. 3400 (1965).
- [25] *Matlab Global Optimization Toolbox User’s Guide*, The MathWorks, Inc., 3rd ed. (2016).
- [26] M. Gutttag and M.C. Boyce, “Locally and Dynamically Controllable Surface Topography Through the Use of Particle-Enhanced Soft Composites,” *Adv. Funct. Mater.* **25**, 3641–3647 (2015).
- [27] H. Meng and G. Li, “A review of stimuli-responsive shape memory polymer composites,” *Polymer* **54**, 2199–2221 (2013).
- [28] Y. Liu, H. Lv, X. Lan, J. Leng, and S. Du, “Review of electro-active shape-memory polymer composite,” *Compos. Sci. Technol.* **69**, 2064–2068 (2009).